Available online at www.sciencedirect.com
ScienceDirect
International Journal of Solids and Structures 44 (2007) 6945–6962
INTERNATIONAL JOURNAL OF SOLIDS AND STRUCTURES
www.elsevier.com/locate/ijsolstr

Micromechanics of elasto-plastic materials reinforced with ellipsoidal inclusions

O. Pierard [a], C. González [b], J. Segurado [b], J. LLorca [b,*], I. Doghri [a]

[a] *Université Catholique de Louvain, CESAME 4 Avenue G. Lemaître, B-1348 Louvain-la-Neuve, Belgium*
[b] *Department of Materials Science, Polytechnic University of Madrid, E. T. S. de Ingenieros de Caminos, 28040 Madrid, Spain*

Received 1 February 2007; received in revised form 16 March 2007
Available online 24 March 2007

Abstract

The effective mechanical behavior of an elasto-plastic matrix reinforced with a random and homogeneous distribution of aligned elastic ellipsoids was obtained by the finite element simulation of a representative volume element (RVE) of the microstructure and by homogenization methods. In the latter, the composite behavior was modeled by linearization of the local behavior through the use of the tangent or secant stiffness tensors of the phases. "Quasi-exact" results for the tensile deformation were attained by averaging of the stress-strain curves coming from the numerical simulation of RVEs containing a few dozens of ellipsoids. These results were used as benchmarks to assess the accuracy of the homogenization models. The best approximations to the reference numerical results were provided by the incremental and the second-order secant methods, while the classical or first-order secant approach overestimated the composite flow stress, particularly when the composite was deformed in the longitudinal direction. The discrepancies among the homogenization models and the numerical results were assessed from the analysis of the stress and strain microfields provided by the numerical simulations, which demonstrated the dominant effect of the localization of the plastic strain in the matrix on the accuracy of the homogenization models.

Keywords: Computational micromechanics; Composite materials; Homogenization; Plasticity; Mean-field models

1. Introduction

Homogenization methods are powerful tools to simulate the mechanical behavior of heterogeneous materials, and in particular of composites, at a very reasonable computational cost. Better and better approximations have been developed over the years, which allow to take into account not only the volume fraction and shape of the phases in the composite but also their spatial distribution (Nemat-Nasser and Hori, 1999; Torquato, 2001), and which provide very accurate predictions for the thermo-elastic properties of linear composites (Segurado and LLorca, 2002). More problematic has been, however, the extension of these methods to the plastic regime in which the strain localization during plastic deformation is more difficult to capture. Since the

* Corresponding author. Tel.: +34 913 365 375; fax: +34 915 437 845.
E-mail address: jllorca@mater.upm.es (J. LLorca).

0020-7683/$ - see front matter
doi:10.1016/j.ijsolstr.2007.03.019

pioneer work of Hill (1965), many extensions of the homogenization methods to the plastic regime have been attempted, and they were reviewed recently in various excellent papers (Ponte-Castañeda and Suquet, 1998; Chaboche et al., 2005). Basically, these methods compute the non-linear composite response by linearization of the local behavior through the use of the tangent (Hill, 1965; Hutchinson, 1970; Petterman et al., 2002), or secant (Tandon and Weng, 1988; Berveiller and Zaoui, 1979; Suquet, 1997) stiffness tensors of the phases or, more recently, by using the tangent stiffness but in a non-incremental form (the "affine" approximation, Masson and Zaoui (1999); Masson et al. (2000)). The overall composite stiffness tensor is computed from those of each phase through the chosen linear approximation.

It was early recognized that the incremental approaches based on the tangent stiffness tensors of the phases overestimated the flow stress of the material, and the origin of this error was traced to the anisotropic nature of the tangent stiffness tensor during plastic deformation. This limitation led to the development of the secant methods, which deal with the elasto-plastic deformation within the framework of non-linear elasticity. Although the overall response was much closer to the real behavior (Tandon and Weng, 1988; Berveiller and Zaoui, 1979), another source of error was detected, particularly in composite materials containing one elastic phase. The plastic strain in the matrix was determined from a reference equivalent stress computed in the classic homogenization models from the volumetric average of the matrix stress tensor. This equivalent stress is, however, significantly lower than the phase average of the equivalent stress because of the large stress gradients which develop during plastic deformation, and hence the composite yield and flow stresses were overestimated. This problem was well-known, and several attempts were made to determine the equivalent stress from energy considerations (Qiu and Weng, 1992) or statistically-based theories (Buryachenko, 1996), which finally led to the so-called "modified" secant approximation (Suquet, 1995), where the reference equivalent stress in the matrix is determined from the volumetric average of second-order moment of the stress tensor in this phase instead of the usual first order moment. An identical theory was developed independently by Ponte-Castañeda (1991) from a different perspective based on the variational properties of a potential which governs the overall composite behavior.

Of course, secant approaches cannot simulate the mechanical behavior under non-proportional loading paths (e.g. cyclic deformation), and this renewed the interest in incremental approaches based on the tangent stiffness tensors. It was found that much better approximation of the flow stress was obtained when only the isotropic part of the tangent stiffness tensors was used in the analyses (Gilormini, 1995; González and LLorca, 2000). More recently, Doghri and Ouaar (2003) have obtained good predictions for the elasto-plastic response of sphere-reinforced composites by using the isotropic version of the stiffness tensor only to compute Eshelby's tensor, while the anisotropic version is used in all the other operations, allowing the study of non-proportional loading paths.

Thus, it is nowadays recognized that current secant and tangent models can deliver acceptable approximations of the overall elasto-plastic response of heterogeneous materials. Nevertheless, their accuracy and range of validity could not be rigorously established in the absence of an "exact" solution, which was not available even for the simple composite system made up of an elasto-plastic matrix reinforced with a random and homogeneous dispersion of elastic spheres. This limitation was recently overcome through the numerical simulation of a Representative Volume Element (RVE) of the microstructure containing several dozens of particles (Segurado et al., 2002, 2003). It was shown that the estimates of the mechanical response in different sphere realizations presented little scatter and that the average value gathered from the simulations was reasonably close (by a few percent) to the exact solution. These results were used in González et al. (2004) and Pierard et al. (2007) to assess the accuracy of the classical and modified secant methods in computing the elasto-plastic deformation of sphere-reinforced composites. It is not clear, however, whether the conclusions of the previous publication can be extended to other reinforcement geometries, such as ellipsoids, and this is the main aim of this investigation. A very precise solution for the tensile response of a composite material made up of a continuous elasto-plastic matrix reinforced with aligned elastic ellipsoids was computed numerically, and the results were compared with those obtained with the current tangent and secant homogenization methods. The ability of each method to reproduce the actual composite behavior was assessed from the analysis of the stress and strain microfields provided by the numerical simulations, which can be integrated over the corresponding volumes to obtain the average values of the field quantities. They were compared with those used by the homogenization models to devise new modifications which can further improve their accuracy.

Throughout the paper, bold lowercase Roman and Greek letters stand for first and second order tensors, respectively, and bold capital letters for fourth order tensors. In addition, the different products are expressed as $(\boldsymbol{A}\,\boldsymbol{\sigma})_{ij} = A_{ijkl}\sigma_{lk}$, $\boldsymbol{A} :: \boldsymbol{B} = A_{ijkl}B_{lkji}$, and $(\boldsymbol{\sigma} \otimes \boldsymbol{\sigma})_{ijkl} = \sigma_{ij}\sigma_{kl}$. Finally, $\bar{\boldsymbol{\sigma}}$ represents the volumetric average of $\boldsymbol{\sigma}$.

2. Microstructure generation

The RVE of the microstructure chosen to simulate the mechanical behavior was a rectangular prism of dimensions $\alpha L \times L \times L$, which contained a random and homogeneous dispersion of non-overlapping identical ellipsoids, aligned in the longer axis of the prism. The prism and the ellipsoids had the same aspect ratio α. Previous investigations (Hazanov and Huet, 1994; Segurado and LLorca, 2002) have demonstrated that better approximations to the effective composite properties are obtained if periodic boundary conditions (instead of constant forces or linear displacements) are applied to the prism faces, and thus a periodic ellipsoid distribution was generated in the RVE.

The length of the ellipsoid longitudinal and transverse semi-axes, ($\alpha \times r$ and r, respectively) were obtained from the volume fraction of ellipsoids in the RVE, ξ and the number of ellipsoids in the prism, N, as

$$r = L\left[\frac{3\xi}{4\pi N}\right]^{1/3} \tag{1}$$

The coordinates of the ellipsoid centers were generated randomly and sequentially using the Random Sequential Adsorption Algorithm (Rintoul and Torquato, 1997). A new inclusion i was accepted if the following conditions were verified:

- The minimum distance between the surface of the ellipsoid i and all the previously generated inclusions $j = 1, \ldots, i-1$ has to be larger than $0.035\alpha r$ to allow for an adequate finite element discretization of the ligament between neighbor inclusions. If the surface of particle i cut any of the prism surfaces, this condition was checked with the ellipsoids near the opposite surface because the microstructure of the RVE was periodic.
- The minimum distance between the surface of the ellipsoid i and the prism faces, edges or corners has to be larger than $0.05\alpha r$ to avoid distorted elements during meshing.

If any of the above conditions was lacking, the ellipsoid was rejected and a new one was generated until the prescribed number of ellipsoids in the prism N was attained. This strategy to generate the RVE needs an efficient algorithm to determine the minimum distance between the surfaces of two non-overlapping ellipsoids and between the ellipsoid surface and the prism faces, edges and corners. There are analytical expressions to compute the minimum distance between an ellipsoid and a plane, and the minimum distance between two ellipsoids is given by the iterative algorithm proposed by Lin and Han (2002). Let $x^k \in \Omega(i)$ and $y^k \in \Omega(j)$ be two points, generated in the iteration k, which belong to the surface of ellipsoids i and j, expressed respectively by $\Omega(i)$ and $\Omega(j)$. Then, two spheres tangent to x^k and y^k, and completely embedded in the ellipsoids i and j, are generated (Fig. 1). The position of the sphere centers, c_i^k and c_j^k, and the sphere radii, r_i^k and r_j^k, are given in Lin and Han (2002). If the segment $[c_i^k, c_j^k]$ between the two centers is entirely contained in the union $i \cup j$, the two ellipsoids overlap. Otherwise, the length of the segment $[x^k, y^k]$ is a candidate for the minimum distance between the ellipsoids, and it can be shown that the condition is fulfilled when the segments $[x^k, y^k]$, $[c_i^k, x^k]$ and $[c_j^k, y^k]$ are parallel. If they are not, two new points x^{k+1} and y^{k+1} are generated as the intersection of

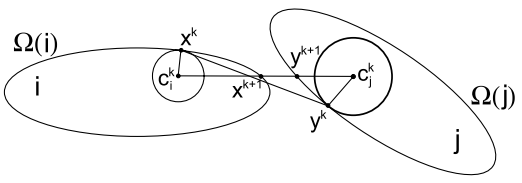

Fig. 1. Determination of the minimum distance between two ellipsoids.

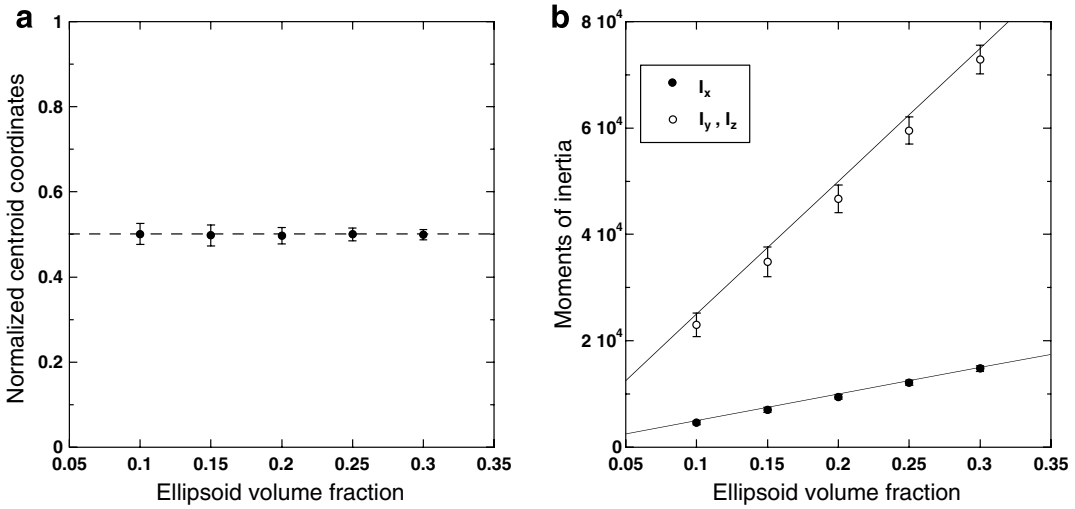

Fig. 2. (a) Coordinates of the centroid of the dispersion of ellipsoids as a function of inclusion volume fraction. (b) Moments of inertia, I, of the aligned ellipsoid distribution in relation to the longitudinal (x) and transverse (y and z) axes as a function of the inclusion volume fraction. The average values and the standard deviations for each volume fraction were obtained from one hundred realizations of 30 aligned ellipsoids. The density was taken equal to 1 to compute the moment of inertia.

the line segment $[c_i^k, c_j^k]$ with the surfaces $\Omega(i)$ and $\Omega(j)$, respectively (Fig. 1) and the whole process is repeated. Convergence to the unique solution of the problem is guaranteed after a finite number of iterations (Lin and Han, 2002). This methodology can be easily extended to compute the distance between the ellipsoid and prism edges and corners.

Two tests were carried out to ensure that the dispersion of the ellipsoids in the RVE led to a statistically homogeneous and transversally isotropic material. One hundred prisms containing a random dispersion of 30 aligned ellipsoids with an aspect ratio $\alpha = 3$ were generated for $\xi = 0.10, 0.15, \ldots, 0.30$. The average position of the centroid (normalized by the prism length) is plotted as a function of the volume fraction of ellipsoids in the RVE together with the corresponding standard deviation, Fig. 2(a). The centroid position is located at the center of the prism, as in a statistically homogeneous dispersion. Moreover, the standard deviation was very small and decreased with the volume fraction of inclusions. The transverse isotropy of the dispersion was checked through the moments of inertia in relation to three perpendicular axes with their origin at the center of the prism. The average values (and the corresponding standard deviations) in relation to the longitudinal axis (x) and two perpendicular axes (y and z) are plotted in Fig. 2(b) as a function of the inclusion volume fraction. The moments of inertia of a homogeneous prism whose mass was equal to the mass of all the ellipsoids in the random arrangement are also plotted for comparison as solid lines in Fig. 2(b). The agreement between the generated microstructures and the exact values for the homogeneous prism is indicative of the transverse isotropy of the RVE. In addition, the differences in the moments of inertia in relation to the y and z axes were negligible.

3. Finite element simulations

The algorithm presented in the previous section was used to create a periodic distribution of aligned ellipsoids with an aspect ratio of 3 in a prismatic cell with the same aspect ratio. Periodic prismatic cells for the numerical analysis were generated by splitting the ellipsoids intersecting the prism faces into the appropriate number of parts which were copied to the opposite faces, leading to the "ellipsoids in box" prism in Fig. 3. Three faces of the prism were meshed with quadratic triangles, and the meshes were copied to the opposite sides to apply the periodic boundary conditions. The volume was meshed using NETGEN (2004) with quadratic tetrahedra (Fig. 3). The standard discretization of the prisms comprised approximately 75000 elements and 110000 nodes. Finer meshes (with over 200000 elements) provided very close results and it was assumed

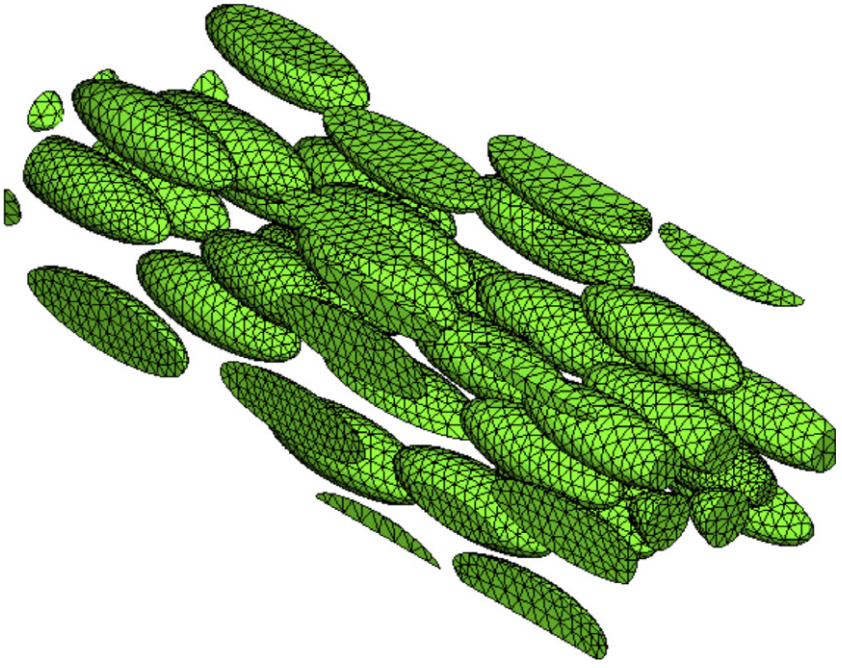

Fig. 3. Periodic prismatic cell showing the "ellipsoids in box" morphology and the finite element discretization of the ellipsoids. The prismatic cell contains 30 aligned ellipsoids with an aspect ratio of 3. $\xi = 0.25$.

that the standard discretization was good enough. The finite element meshes always included at least two elements of matrix between neighbor ellipsoids. It should be mentioned that serious difficulties were found to discretize microstructures with ellipsoids with an aspect ratio larger than 3. Of course, short fibers (with an aspect ratio of $\approx$10) could be approximated by cylinders with hemispherical caps but they are not equal to ellipsoids, and this difference would have hindered the comparison with Eshelby-based mean-field methods.

The model volume (matrix and inclusions) was meshed using modified 10-node tetrahedra (C3D10M in Abaqus (2005)) with integration at four Gauss points and hourglass control. This modified tetrahedron exhibits minimal volumetric locking during plastic straining and captures better than the standard 10-node tetrahedron the strain gradients in the matrix between the inclusions because it has three extra internal degrees of freedom.

Periodic boundary conditions were applied to the prismatic cell as

$$\begin{aligned} \boldsymbol{u}(x,y,0) - \boldsymbol{u}_z &= \boldsymbol{u}(x,y,L) \\ \boldsymbol{u}(x,0,z) - \boldsymbol{u}_y &= \boldsymbol{u}(x,L,z) \\ \boldsymbol{u}(0,y,z) - \boldsymbol{u}_x &= \boldsymbol{u}(\alpha L,y,z) \end{aligned} \tag{2}$$

where $\boldsymbol{u}$ stands for the displacement vector in the different prism faces and the vectors $\boldsymbol{u}_x$, $\boldsymbol{u}_y$ and $\boldsymbol{u}_z$ depend on the particular loading applied to the cell. Tensile deformation ϵ_x along the longitudinal axis is given by $\boldsymbol{u}_x = (\epsilon_x \alpha L, 0, 0)$, $\boldsymbol{u}_y = (0, u_y, 0)$ and $\boldsymbol{u}_z = (0,\ 0, u_z)$, in which u_y and u_z are computed from the conditions

$$\int_\Omega T_y \,\mathrm{d}\Omega = 0 \text{ on } y = L \quad \text{and} \quad \int_\Omega T_z \,\mathrm{d}\Omega = 0 \text{ on } \quad z = L \tag{3}$$

where T_y and T_z stand for the normal tractions acting on the prism faces contained in the transverse planes $y = L$ and $z = L$. Similar boundary conditions can be applied to compute the tensile deformation in the transverse direction.

The finite element simulations were done with Abaqus/Standard (2005) within the framework of the small displacements theory. The ellipsoidal inclusions behaved as elastic, isotropic solids characterized by the shear modulus $\mu_i = 166.67$ GPa and the bulk modulus $k_i = 222.22$ GPa. The matrix was modelled as an isotropic

elasto-plastic solid following the von Mises criterion with isotropic hardening. The matrix elastic constants were $\mu_m = 26.32$ GPa and $k_m = 68.63$ GPa, and the von Mises equivalent stress, σ_m^{eq}, was related to the accumulated plastic strain, ϵ_m^p, according to

$$\sigma_m^{eq} = A[\epsilon_m^p]^n \tag{4}$$

where $A = 400$ MPa was the strength coefficient and n the matrix strain hardening exponent. The elastic constants are representative of an Al alloy reinforced with stiff ceramic (alumina, silicon carbide) particles, whereas Eq. (4) provides a wide range of flow stresses, also sensible for aluminum and its alloys.

4. Homogenization techniques

As indicated in the introduction, secant and tangent approaches are the most common homogenization techniques to simulate the non-linear deformation of composite materials. Their implementation in the case of a composite material made up of an elasto-plastic matrix reinforced with elastic, aligned ellipsoids is briefly summarized in this section, as the details of each approach will control the accuracy of the predictions.

4.1. Secant approaches

Secant approaches simulate the non-linear behavior of the composite material and of each phase within the framework of the deformation theory of plasticity. The isotropic, linear elastic behavior of the ellipsoidal inclusions is included as

$$\boldsymbol{\varepsilon}_i = \boldsymbol{M}_i \boldsymbol{\sigma}_i \quad \text{with} \quad \boldsymbol{M}_i = \frac{1}{3k_i}\boldsymbol{J} + \frac{1}{2\mu_i}\boldsymbol{K} \tag{5}$$

where $\boldsymbol{\varepsilon}_i$ and $\boldsymbol{\sigma}_i$ stand for the inclusion strain and stress tensors, $\boldsymbol{M}_i$ is the elastic compliance tensor of the inclusions, and $\boldsymbol{J}$ and $\boldsymbol{K}$ are the fourth-order volumetric and deviatoric projections tensors, respectively. The elasto-plastic behavior of the matrix is introduced by means of the secant compliance tensor, $\boldsymbol{M}_m^s$, and the stresses and strains in the matrix are related by

$$\boldsymbol{\varepsilon}_m = \boldsymbol{M}_m^s \boldsymbol{\sigma}_m \quad \text{with} \quad \boldsymbol{M}_m^s = \frac{1}{3k_m}\boldsymbol{J} + \frac{1}{2\mu_m^s}\boldsymbol{K} \tag{6}$$

where μ_m^s is the secant shear modulus of the matrix, which is a function of the von Mises equivalent stress, σ_m^{eq}, according to

$$\mu_m^s = \frac{\sigma_m^{eq}\mu_m}{\sigma_m^{eq} + 3\mu_m\epsilon_m^p} \quad \text{with} \quad \epsilon_m^p = \left[\frac{\sigma_m^{eq}}{A}\right]^{1/n} \tag{7}$$

The effective (or volume-averaged) strain and stress tensors in the composite material $\bar{\boldsymbol{\varepsilon}}$ and $\bar{\boldsymbol{\sigma}}$ are related univocally by the secant effective compliance tensor (Berveiller and Zaoui, 1979; Tandon and Weng, 1988)

$$\bar{\boldsymbol{\varepsilon}} = \boldsymbol{M}^s(\sigma_m^{eq})\ \bar{\boldsymbol{\sigma}} \tag{8}$$

where σ_m^{eq} is a reference equivalent stress in the matrix, which has to be computed from the first or second order moment of the stress tensor in the matrix as indicated below.

$\boldsymbol{M}^s$ can be determined assuming linear homogenization and, in the case of a two-phase material, it is expressed by

$$\boldsymbol{M}^s = (1-\xi)\boldsymbol{M}_m^s\boldsymbol{B}_m^s + \xi\boldsymbol{M}_i\boldsymbol{B}_i^s \tag{9}$$

where $\boldsymbol{B}_m^s$ and $\boldsymbol{B}_i^s$ stand for the corresponding secant stress concentration tensors for the matrix and the inclusions, which relate the average stress in the composite with the average stresses in each phase according to

$$\bar{\boldsymbol{\sigma}}_m = \boldsymbol{B}_m^s\ \bar{\boldsymbol{\sigma}} \quad \text{and} \quad \bar{\boldsymbol{\sigma}}_i = \boldsymbol{B}_i^s\ \bar{\boldsymbol{\sigma}} \tag{10}$$

The stress concentration tensors can be approximated using any linear homogenization scheme, and the Mori-Tanaka method was selected because it is easy to implement and provides accurate results for aligned ellipsoids (Benveniste, 1987). Thus,

$$\boldsymbol{B}_i^{\mathrm{s}} = [\boldsymbol{I} + (1-\xi)(\boldsymbol{M}_m^{\mathrm{s}})^{-1}(\boldsymbol{I}-\boldsymbol{S}_i)(\boldsymbol{M}_i - \boldsymbol{M}_m^{\mathrm{s}})]^{-1} \tag{11}$$

$$\boldsymbol{B}_m^{\mathrm{s}} = \frac{1}{1-\xi}(\boldsymbol{I} - \xi \boldsymbol{B}_i^{\mathrm{s}}) \tag{12}$$

in which $\boldsymbol{S}_i$ is Eshelby's tensor for an ellipsoidal elastic inclusion. $\boldsymbol{S}_i$ depends on the inclusion aspect ratio α and on the secant Poisson's ratio of the matrix, ν_m^{s}, and the components of the Eshelby's tensor are given explicitly in Appendix A.

Eqs. (5)–(12) are a non-linear set of algebraic equations in σ_m^{eq}, which have to be solved for each value of the applied stress $\bar{\boldsymbol{\sigma}}$ to determine the secant effective compliance tensor of the composite and thus the effective composite strain $\bar{\boldsymbol{\varepsilon}}$ through Eq. (8). From the practical viewpoint, this set is solved using a fixed point algorithm, which begins with a trial value of the secant compliance tensor of the matrix (the one computed in the previous loading step).

Two variations of this method have been developed and they differ in the way the reference equivalent stress in the matrix is computed. In the classical approach (or first order method), the reference equivalent stress in the matrix, $\hat{\sigma}_m^{\mathrm{eq}}$, was determined as

$$\hat{\sigma}_m^{\mathrm{eq}} = \left[\frac{3}{2}(\boldsymbol{K}\bar{\boldsymbol{\sigma}}_m)(\boldsymbol{K}\bar{\boldsymbol{\sigma}}_m)\right]^{1/2} \tag{13}$$

while in the modified (or second order method) it is computed from the second order moment of the effective stress in the matrix as (Ponte-Castañeda, 1991; Suquet, 1995)

$$\hat{\bar{\sigma}}_m^{\mathrm{eq}} = \left[\frac{3}{2}\boldsymbol{K} :: (\overline{\boldsymbol{\sigma}_m \otimes \boldsymbol{\sigma}_m})\right]^{1/2} \tag{14}$$

and analytical expressions to compute $\hat{\bar{\sigma}}_m^{\mathrm{eq}}$ were given in Suquet (1997) for the case of a sphere-reinforced composite. The extension to ellipsoidal inclusions is detailed in the Appendix B.

4.2. Incremental approach

The incremental approach is another option to predict both the macroscopic and per-phase response of non-linear materials. Although the numerical implementation is more complex, incremental models can take into account rigorously the effect of the loading history on the deformation. The behavior of the material is computed through a step-by-step incremental procedure by linearizing the local constitutive laws written in rate-form, so homogenization models valid in linear elasticity can apply in each time interval. Given the state of deformation at the beginning of a time step, the effective stress ($\Delta\bar{\boldsymbol{\sigma}}$) and strain ($\Delta\bar{\boldsymbol{\varepsilon}}$) increments during the time interval are related by

$$\Delta\bar{\boldsymbol{\sigma}} \approx \boldsymbol{L}^{\mathrm{t}}(\sigma_m^{\mathrm{eq}})\Delta\bar{\boldsymbol{\varepsilon}} \tag{15}$$

in which $\boldsymbol{L}^{\mathrm{t}}$ stands for an instantaneous elasto-plastic tangent modulus tensor which depends on the von Mises equivalent stress in the matrix, as computed from the volume-averaged matrix stress tensor (Eq. (13))[1].

Similar to the secant approach, the effective tangent operator $\boldsymbol{L}^{\mathrm{t}}$ can be obtained as

$$\boldsymbol{L}^{\mathrm{t}} = (1-\xi)\boldsymbol{L}_m^{\mathrm{t}}\boldsymbol{A}_m^{\mathrm{t}} + \xi \boldsymbol{L}_i \boldsymbol{A}_i^{\mathrm{t}} \tag{16}$$

where $\boldsymbol{L}_m^{\mathrm{t}}$ is the consistent (or algorithmic) tangent operator which relates the stress and strain increments in the matrix over the time interval, and $\boldsymbol{A}_m^{\mathrm{t}}$ and $\boldsymbol{A}_i^{\mathrm{t}}$ stand for the tangent strain concentration tensors which link the average strain increment in the composite to those in the phases according to

[1] Extension of the incremental approaches to compute the von Mises equivalent stress in the matrix from the second order moment of the matrix stress tensor is still an open subject.

$$\Delta\boldsymbol{\varepsilon}_m = \boldsymbol{A}_m^{\mathrm{t}}\Delta\bar{\boldsymbol{\varepsilon}}, \qquad \Delta\boldsymbol{\varepsilon}_i = \boldsymbol{A}_i^{\mathrm{t}}\Delta\bar{\boldsymbol{\varepsilon}} \tag{17}$$

and they are expressed by the following equations when the Mori-Tanaka linear homogenization scheme is used:

$$\boldsymbol{A}_i^{\mathrm{t}} = [\boldsymbol{I} + (1-\xi)\boldsymbol{S}_i(\boldsymbol{L}_m^{\mathrm{t}})^{-1}(\boldsymbol{L}_i - \boldsymbol{L}_m^{\mathrm{t}})]^{-1} \tag{18}$$

$$\boldsymbol{A}_m^{\mathrm{t}} = \frac{1}{1-\xi}(\boldsymbol{I} - \xi\boldsymbol{A}_i^{\mathrm{t}}) \tag{19}$$

The consistent tangent operator $\boldsymbol{L}_m^{\mathrm{t}}$ can be computed analytically for most constitutive models. In the case of the J_2 elasto-plastic model considered here, it is given by Doghri and Ouaar (2003)

$$\boldsymbol{L}_m^{\mathrm{t}} = \boldsymbol{L}_m^{\mathrm{ep}} - \frac{(2\mu_m)^2(\Delta\epsilon_m^{\mathrm{p}})}{\sigma_m^{\mathrm{eq,tr}}}\left[\frac{3}{2}\boldsymbol{K} - \boldsymbol{n}\otimes\boldsymbol{n}\right] \tag{20}$$

where $\sigma_m^{\mathrm{eq,tr}}$ a trial (elastic predictor) of the equivalent stress at the end of the considered time step, and $\boldsymbol{L}_m^{\mathrm{ep}}$ is the so-called continuum elasto-plastic tangent operator ($\dot{\boldsymbol{\sigma}}_m = \boldsymbol{L}_m^{\mathrm{ep}}\dot{\boldsymbol{\varepsilon}}_m$) which is expressed as

$$\boldsymbol{L}_m^{\mathrm{ep}} = \boldsymbol{L}_m - \frac{4\mu_m^2}{3\mu_m + nA[\epsilon_m^{\mathrm{p}}]^{n-1}}\boldsymbol{n}\otimes\boldsymbol{n} \tag{21}$$

where $\boldsymbol{L}_m$ is the matrix elastic stiffness tensor, and $\boldsymbol{n}$ the normal to the yield surface in stress space

$$\boldsymbol{n} = \frac{3}{2}\frac{\boldsymbol{K}\boldsymbol{\sigma}_m}{\sigma_m^{\mathrm{eq}}} \tag{22}$$

It should be noted that $\boldsymbol{L}_m^{\mathrm{t}} \to \boldsymbol{L}_m^{\mathrm{ep}}$ for vanishingly small plastic strain increments and that both tangent operators are anisotropic during a plastic strain increment. In order to avoid the stiff response associated with incremental models when the anisotropic form of the tangent operator is used in the analysis (Gilormini, 1995; González and LLorca, 2000), Eshelby's tensor $\boldsymbol{S}_i$ was computed with an isotropic part of $\boldsymbol{L}_m^{\mathrm{t}}$ while the anisotropic version is used in all the other operations (see Doghri and Ouaar (2003)). This approximation provides a softer response and allows the simulation of non-proportional loading paths. Eqs. (15)–(22) stand for a set of non-linear equations which are solved following a fixed point iterative scheme starting from a given macroscopic strain increment over the time step.

5. Results and discussion

5.1. Accuracy of the numerical simulations

Theoretical studies have demonstrated that the critical size of the RVE to obtain a size-independent response is small in the case of isotropic composites reinforced with randomly-oriented ellipsoidal inclusions in the elastic regime (Monetto and Drugan, 2004): a few dozens of ellipsoids in the RVE can provide an accurate estimation (up to a few percent) of the elastic constants. There are no theoretical estimations of the minimum RVE size for non-isotropic composites and/or non-linear materials, and the accuracy of the numerical simulations has to be established by comparing the results obtained with RVE of various sizes or by the scatter in the effective properties given by different dispersions of reinforcements. The former technique was used in Gusev et al. (2000) and Hine et al. (2002) for the elastic properties of uniaxially-reinforced composites and the latter in Segurado et al. (2002), Segurado et al. (2003), and Pierard et al. (2007) for the plastic and viscoplastic deformation of sphere-reinforced materials. Both analyses concluded that RVE containing 25–50 particles/fibers were large enough to limit the error in the effective properties to a few percent and this value decreased rapidly by averaging the results of several realizations. These conclusions were checked in the case of ellipsoidal reinforcements by generating four prismatic cells with homogeneous and isotropic distributions of 5, 15, 30 and 40 aligned ellipsoids with an aspect ratio of 3. The prism aspect ratio also was 3 and the ellipsoid volume fraction was 25%. The stress–strain curve in tension was simulated along the longitudinal direction and the average curves for each set of cells with the same number of inclusions are plotted in Fig. 4, together with the corresponding standard deviation for the cells with 5 and 30 ellipsoids. The numerical results were prac-

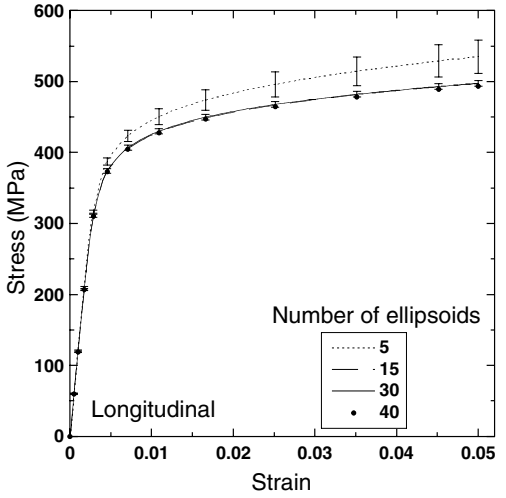

Fig. 4. Average stress-strain curves in tension along the longitudinal direction for prismatic cells containing 5, 15, 30 and 40 aligned ellipsoids. Each curve is the average of four simulations. The ellipsoid volume fraction was 25%. The error bars in the simulations with 5 and 30 ellipsoids stand for the standard deviation. The ellipsoid and matrix properties can be found in the text.

tically superimposed in the elastic region but, as it was expected, significant differences were found from the onset of plastic deformation. Nevertheless, the average stress-strain curves obtained with 15, 30 or 40 ellipsoids were almost superimposed and the standard deviation decreased rapidly with the number of ellipsoids in the prismatic cell. It was just 1% in the cells with 30 ellipsoids, and it was assumed these cells were large enough to represent the effective properties of the composite in the plastic regime.

Following these results, the four homogeneous and isotropic distributions of 30 aligned ellipsoids were used to compute the reference effective properties of the composite. They were deformed in tension along the longitudinal and transverse directions, leading to 4 stress–strain curves in the longitudinal direction and to 8 in the transverse one for each set of material properties. The longitudinal ones are plotted in Fig. 5(a) and those perpendicular to the main axis of the ellipsoids in Fig. 5(b) for the composites with $n = 0.05$ and 0.40. All the curves coincided until plastic flow became dominant, and it was found that the scatter in the transverse direction was higher than in the longitudinal one. The maximum differences at an applied strain of 0.05 were lim-

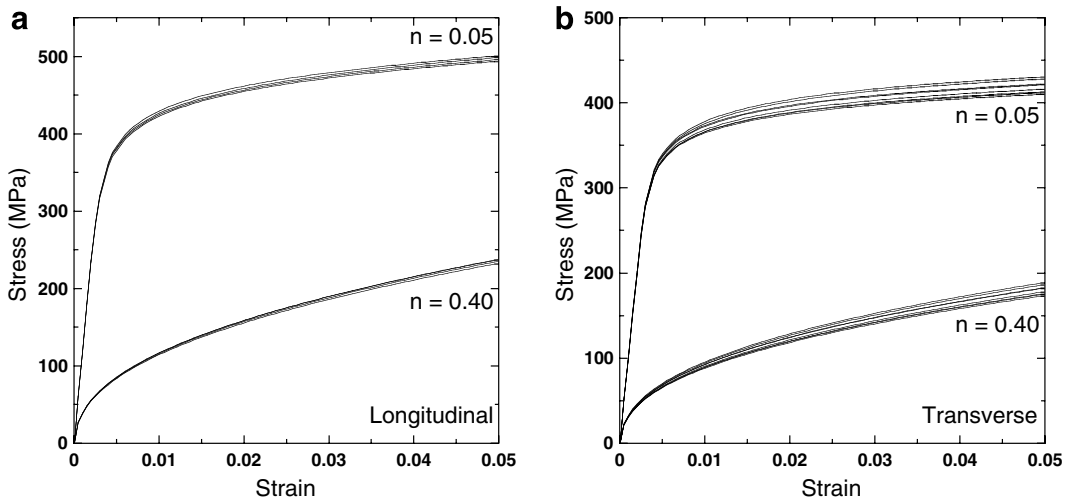

Fig. 5. Uniaxial stress–strain curves in tension of the composite reinforced with 25 volume % of aligned ellipsoids. (a) Longitudinal deformation (b) transverse deformation.

ited, however, to 4.8% and 1.7%. Thus, the stress-strain curves obtained on averaging the 8 simulations along the transverse direction and the 4 simulations along the longitudinal one can be considered very close (to a few percent) to the solution for the boundary value problem, and can be used as a benchmark to check the accuracy of the homogenization methods in the elasto-plastic regime.

5.2. Comparison with homogenization models

The tensile stress–strain curves in the longitudinal and transverse directions predicted by the homogenization models are plotted in Figs. 6 and 7, respectively. They include the results of the two secant models (in which the reference stress in the matrix is computed from the volumetric average of the first or second order moment of the matrix stress tensor) and the incremental method as well as the reference behavior obtained by averaging the stress–strain curves provided by the finite element simulations. Figs. 6(a) and 7(a) show the

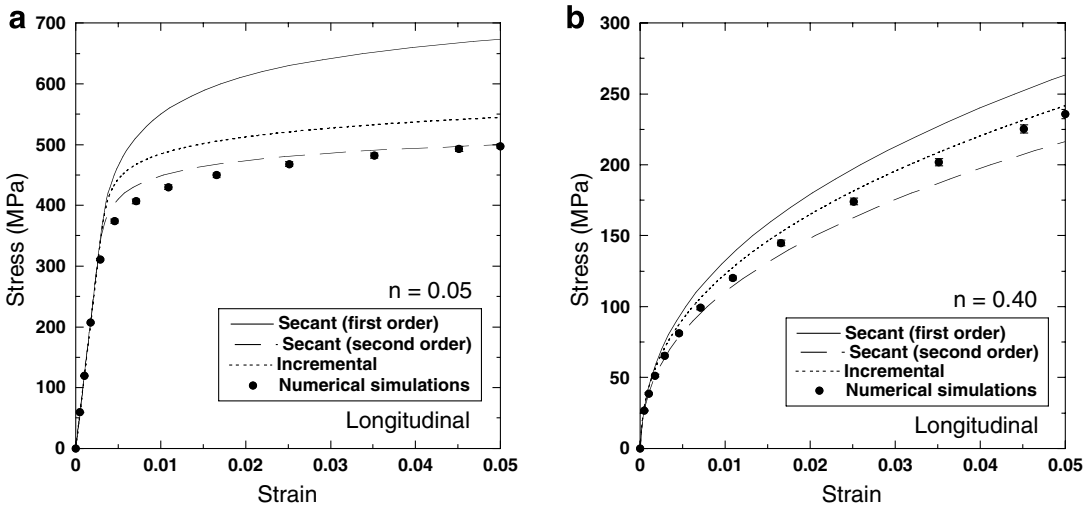

Fig. 6. Predictions of the tensile stress-strain curves in the longitudinal direction for the composite reinforced with 25 volume % of aligned ellipsoids. (a) $n = 0.05$ (b) $n = 0.40$. The error bars represent the standard deviation on the numerical simulations.

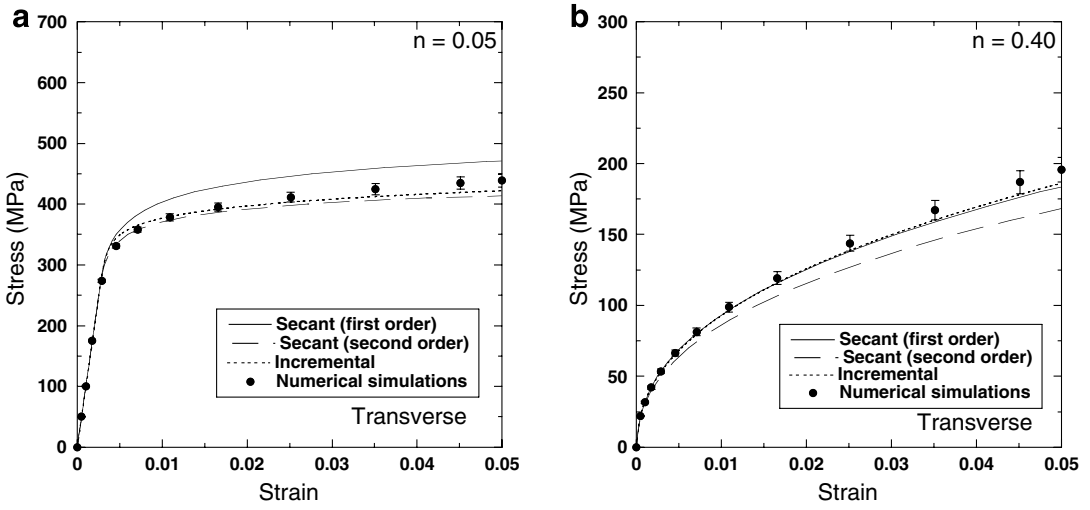

Fig. 7. Predictions of the tensile stress–strain curves in the transverse direction for the composite reinforced with 25 volume % of aligned ellipsoids. (a) $n = 0.05$ (b) $n = 0.40$. The error bars represent the standard deviation on the numerical simulations.

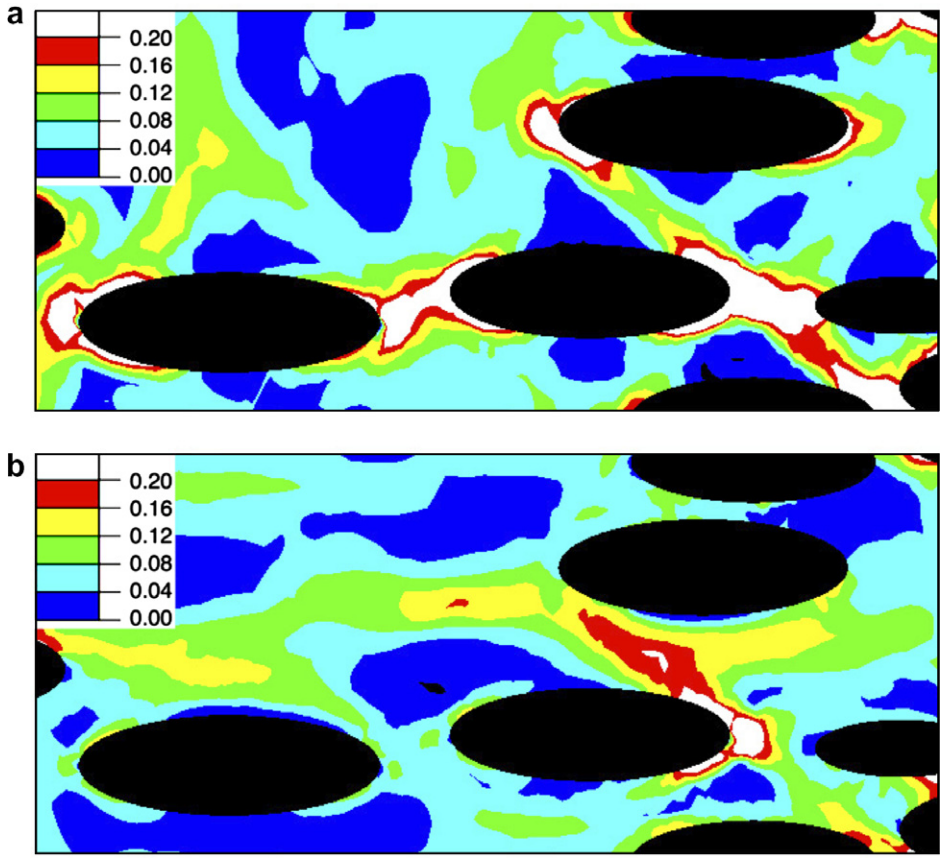

Fig. 8. Contour plot of the accumulated plastic strain in the matrix after tensile deformation up to 5% in the composite with $n = 0.05$. (a) Longitudinal deformation (b) transverse deformation.

curves when the matrix strain hardening coefficient was 0.05 and Figs. 6(b) and 7(b) present the results when $n = 0.40$. A comparison of the secant models showed that the first order method always provided a stiffer response, which overestimated the benchmark numerical results when the composite was deformed in the longitudinal direction. Moreover, the differences between the first and second order estimates increased as the strain hardening exponent of the matrix decreased. It is evident that both factors (deformation axis and matrix strain hardening exponent) influenced the deformation patterns in the matrix, which are shown in Fig. 8(a) and (b) for the material deformed up to 5% in the longitudinal and transverse direction. The stress concentrations in the matrix were maximum between the ends of elongated ellipsoids aligned in the loading direction, and the localization of the matrix plastic deformation was higher when the composite was loaded in the longitudinal direction.

As the average value of the plastic strain in the matrix was very similar in all the models in Figs. 6 and 7, the degree of heterogeneity in the matrix plastic strain can be assessed by the probability that the plastic strain in the matrix does not exceed a certain value. This cumulative probability was computed from the magnitude of the matrix plastic strain at each Gauss point in each finite element model for a far-field applied strain of 5%, and is plotted in Fig. 9. The curves show that the widest distribution (indicative of maximum heterogeneity in the matrix plastic strain) was found in the composite with $n = 0.05$ deformed in the longitudinal direction, in perfect agreement with the contour plots in Fig. 8. The narrowest one was in the material with $n = 0.40$ deformed perpendicularly to the longest axis of the ellipsoids.

Homogenization methods do not have access to the local values of the stresses in the phases and cannot compute exactly the volumetric average of the equivalent stress in the matrix. Instead they compute an approximate value from the volumetric-average of the stress tensor or of the second order moment of the

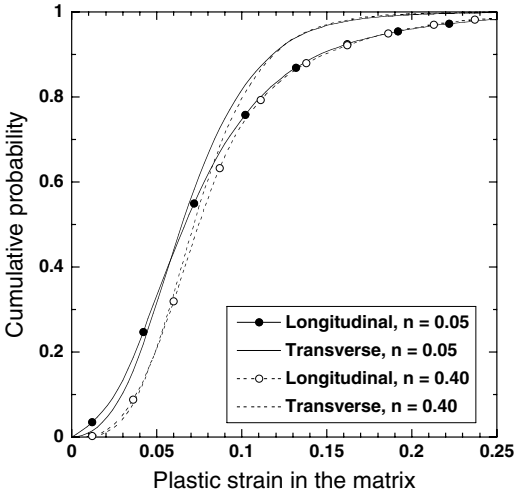

Fig. 9. Cumulative probabilities of the plastic strain in the matrix as a function of the loading direction and of the matrix strain hardening exponent at a far-field applied strain of 5%.

stress tensor. The accuracy of these predictions can be assessed from the results of the numerical simulations, which give the exact volumetric-average of the equivalent stress in the matrix, $\bar{\sigma}_m^{\mathrm{eq}}$, and the estimations provided by the first and second order approaches ($\hat{\sigma}_m^{\mathrm{eq}}$ and $\hat{\hat{\sigma}}_m^{\mathrm{eq}}$). In particular, $\bar{\sigma}_m^{\mathrm{eq}}$ is given by

$$\bar{\sigma}_m^{\mathrm{eq}} = \left[\sum_k \left[\frac{3}{2}(\boldsymbol{K}\boldsymbol{\sigma}_k)(\boldsymbol{K}\boldsymbol{\sigma}_k)\right]^{1/2} V_k\right] \Big/ \left[\sum_k V_k\right] \tag{23}$$

where $\boldsymbol{\sigma}_k$ and V_k stand, respectively, for the stress tensor and the volume associated to the Gauss point k in the finite element discretization of the matrix. The volume-averaged stress tensor, $\bar{\boldsymbol{\sigma}}_m$, and the volume-averaged second-order moment of the stress tensor in the matrix, $\overline{\boldsymbol{\sigma}_m \otimes \boldsymbol{\sigma}_m}$, can be computed as

$$\bar{\boldsymbol{\sigma}}_m = \left[\sum_k \boldsymbol{\sigma}_k V_k\right] \Big/ \sum_k V_k \quad \text{and} \quad \overline{\boldsymbol{\sigma}_m \otimes \boldsymbol{\sigma}_m} = \left[\sum_k (\boldsymbol{\sigma}_k \otimes \boldsymbol{\sigma}_k) V_k\right] \Big/ \sum_k V_k \tag{24}$$

They can be used to determine $\hat{\sigma}_m^{\mathrm{eq}}$ and $\hat{\hat{\sigma}}_m^{\mathrm{eq}}$ using Eqs. (13) and (14). The actual value of the reference stress in the matrix together with the estimations provided by the first and second-order models are plotted in Fig. 10(a) and (b) for the composite deformed in the longitudinal and transverse directions, respectively. They show that the reference stress computed from the second order moment of matrix stress tensor was always extremely close to the exact volumetric average, while the predictions of the first order method were considerably lower. As expected, the maximum differences were found in the situations with maximum strain gradients, i.e. longitudinal deformation and $n = 0.05$. Thus, the predictions of the composite flow stress given by the classical secant method were always stiffer because the matrix von Mises equivalent stress computed from the volume-averaged stress tensor is always lower than that obtained from the volumetric average of the second order moment of the stress tensor. Moreover, these findings are in agreement with the results plotted in Figs. 6 and 7, which show that the predictions of the second-order secant model were closer to the numerical results in the composites loaded in the longitudinal direction or if the strain hardening coefficient of the matrix was low. However, the stress concentrations formed at the end of the elongated ellipsoids when loaded in the longitudinal direction increased tremendously the localization of the plastic strain in the matrix, and the predictions of the classical secant model overestimated the benchmark numerical results.

The composite stress–strain curves obtained using the incremental method are also plotted in Figs. 6 and 7. The incremental approach consistently led to a response in between the predictions of the first and second-order secant models (except for transverse tension and $n = 0.40$—Fig. 7(b)), which was particularly close to the numerical results when the composite was loaded in the transverse direction. The incremental method

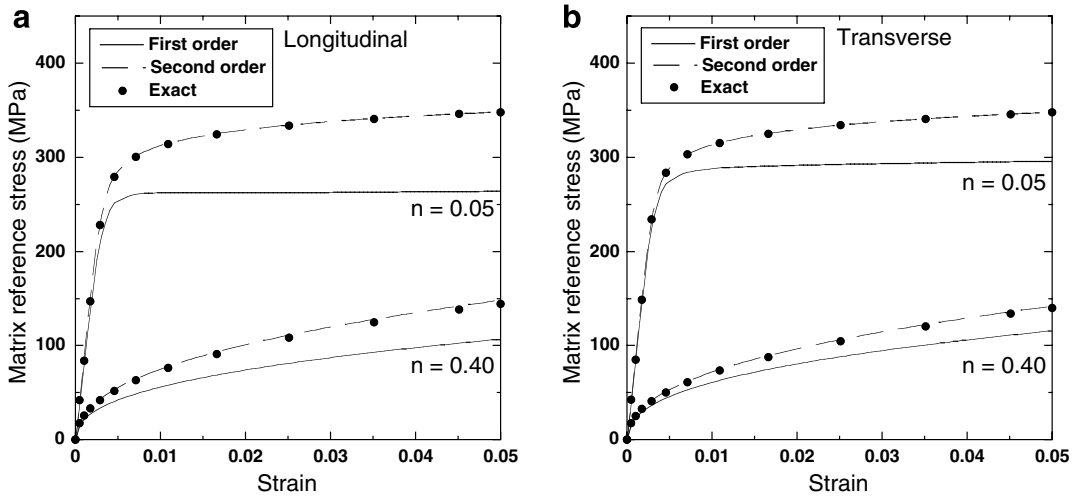

Fig. 10. Evolution of the actual volume-averaged reference stress in the matrix ($\bar{\sigma}_m^{eq}$) as a function of the applied strain and of the estimation based on the volume-averaged first ($\hat{\sigma}_m^{eq}$) and second-order ($\hat{\hat{\sigma}}_m^{eq}$) moment of the matrix stress tensor. (a) Longitudinal deformation. (b) Transverse deformation.

overestimated the flow stress in the longitudinal direction, but the differences from the numerical simulations were only significant when the matrix strain hardening coefficient was 0.05, so both the matrix behavior and the loading direction enhanced the strain localization in the matrix. Thus, the incremental formulation provided excellent predictions for the effective elasto-plastic properties and this result was somewhat surprising because the reference stress in the matrix was computed using the volumetric-average of the stress tensor, and should lead to an overestimation of the flow stress. The softer behavior predicted by the incremental method (which leads to a response close to the reference numerical results in many cases) is related to the use of an isotropic approximation of the (anisotropic) tangent stiffness tensor to compute the Eshelby's tensor.

These results support the use of the incremental method to simulate the plastic deformation of composites instead of the secant approaches because they are more general and provide the same degree of accuracy. In particular, secant approaches serve to simulating only monotonic and proportional loadings at macro and micro levels (cyclic loading is not possible, for instance) and the behavior of each phase should be isotropic. This precludes the use of other plasticity formulations (Hill's model or non-linear kinematic hardening), while the incremental method, although more expensive computationally and more difficult to implement, is not subject to these limitations.

It should be noted finally that the agreement in the predictions at the macroscopic level does not guarantee that the stress and strain fields in each phase are also accurately computed by the models. The simulations carried out in the longitudinal direction in the composite with $n = 0.40$, Fig. 6(b), can be used as an example of this statement. The evolution of the average plastic strain in the matrix is plotted as a function of the applied strain in Fig. 11(a) for this material and loading condition. The homogenization models systematically underestimated the plastic strain in the matrix, as they cannot model adequately the strain localization in the matrix. Underestimation of the matrix plastic strain implies that the matrix hardening rate (and thus the composite flow stress) will be overestimated. This is avoided in the incremental method by using an isotropic approximation of the matrix tangent stiffness tensor and in the secant method by using the second order moment of the matrix stress tensor to compute the reference stress in the matrix. Both approaches reduce the matrix strain hardening and lead to better approximations of the overall composite flow stress, but the mechanical equilibrium condition forces the average stress in the ellipsoids to be underestimated. This is shown in Fig. 11, in which the volumetric average of the von Mises equivalent stress in the ellipsoids is plotted as a function of the applied strain. While the first order secant model provided an acceptable approximation to the von Mises equivalent stress in the ellipsoids, the other two models gave erroneous predictions for the reinforcement stresses. Similar trends were found in the rest of the simulations but they are not detailed here for

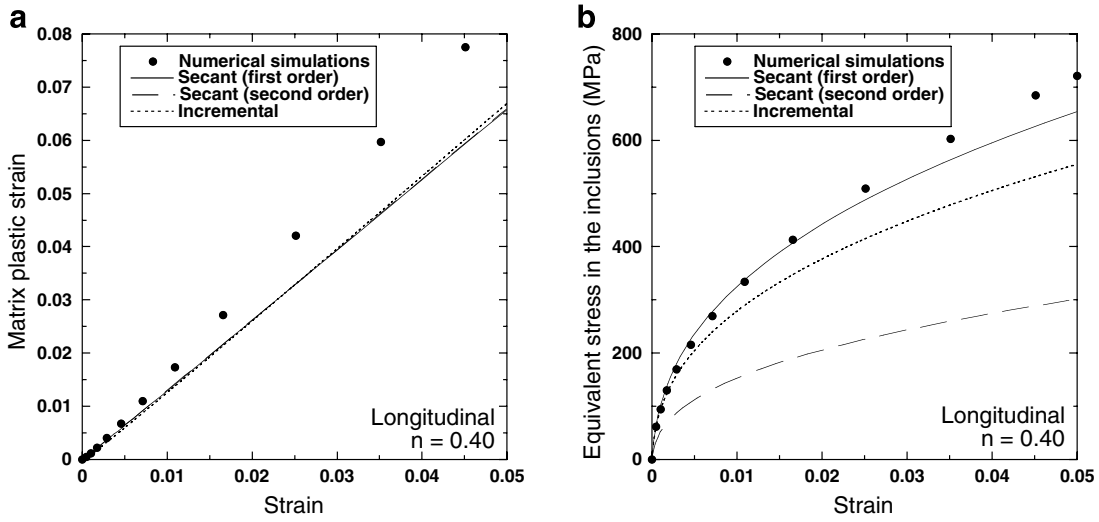

Fig. 11. (a) Evolution of the plastic strain in the matrix as a function of the applied strain. (b) Evolution of the von Mises equivalent stress in the ellipsoids as a function of the applied strain. The composite was loaded in the longitudinal direction and the matrix strain hardening coefficient was 0.40.

the sake of brevity, and it is important to realize that homogenization methods can give accurate predictions of the effective properties but this does not guarantee the same accuracy at the phase level. This has important consequences in modeling damage by either inclusions fracture or interface decohesion with homogenization techniques, and so is important to validate the homogenization predictions with numerical results obtained by computational micromechanics (LLorca and Segurado, 2004; Segurado and LLorca, 2005, 2006).

6. Conclusions

The deformation in uniaxial tension of a model composite made up of a random and homogeneous dispersion of aligned, elastic ellipsoids embedded in an elasto-plastic matrix was simulated by means of computational micromechanics and homogenization methods. In the first approach, the effective properties of the composite were obtained by finite element analysis of an RVE of the microstructure. In the second approach, the non-linear composite behavior was modeled by linearization of the local behavior through the use of the tangent or secant stiffness tensors of the phases. The overall composite stiffness tensor was computed from those of each phase by the Mori-Tanaka approximation.

Numerical simulations carried out with RVEs of different sizes (and thus with different numbers of ellipsoids) showed that a "quasi-exact" result could be obtained by averaging the stress-strain curves of RVEs containing a few dozen ellipsoids. This technique was used to determine the effective elasto-plastic response of a composite containing 25% of ellipsoids in the longitudinal and transverse directions for two different values of the matrix strain hardening exponent (0.05 and 0.40). These results were used as benchmarks to show the accuracy of the predictions of the homogenization methods for composites reinforced with ellipsoids with a moderate aspect ratio of 3. Moreover, the ability of the tangent and secant approaches to reproduce the actual composite behavior was assessed at a deeper level from the analysis of the stress and strain microfields provided by the numerical simulations, which can be integrated over the corresponding volumes to obtain the average values of the field quantities. Overall, the best approximations to the numerical results were provided by the incremental (Doghri and Ouaar, 2003) and the second order secant (Ponte-Castañeda, 1991; Suquet, 1995) methods, while the first order secant method provided a very stiff response. The incremental method led to accurate stress-strain curves in most cases, and tended to overestimate the composite flow stress when the localization of the plastic strain in the matrix was maximum (longitudinal deformation with matrix strain hardening exponent of 0.05). The results of the second order secant method underestimated the reference numerical stress–strain curve only if the localization of the plastic strain in the matrix was minimum (trans-

verse loading and matrix strain hardening exponent of 0.40), giving very good estimations in all other situations. In addition, comparison of the volumetric-average fields in each phase showed that accurate predictions of the effective properties by the homogenization methods did not guarantee the same accuracy at the phase level. The origin of these discrepancies and the modifications of the homogenization methods to improve the predictions in the behavior of each phase will be studied in future. Finally, it should be noted that the results of this paper and of previous investigations (González et al., 2004) seem to indicate that predictions of first-order homogenization models (both incremental and secant formulations) become less accurate as the aspect ratio increases. Nevertheless, definitive conclusions cannot be obtained because of the lack of data for oblate ellipsoids as well as prolate ellipsoids with longer aspect ratio.

Acknowledgements

This investigation was supported by the Spanish Ministry of Education and Science through grant MAT 2006-2602 and by the Comunidad de Madrid through the program ESTRUMAT-CM (reference MAT/0077). The incremental formulation results were obtained with the Digimat software (DIGIMAT, 2005) from e-Xstream engineering. Free access to the software is gratefully acknowledged as well as the support to O.P. of the FNRS for a FRIA scholarship and of the Communauté française de Belgique for a three month stay grant at the Polytechnic University of Madrid.

Appendix A. Eshelby's tensor

The components of Eshelby's tensor for an elastic ellipsoidal inclusion of aspect ratio $\alpha = a/b$ with the axis of length $2a$ parallel to the 1 axis embedded in an isotropic elastic matrix are (Eshelby, 1957)

$$
\begin{aligned}
S_{1111} &= \frac{1}{2(1-\nu_m)}\left[\frac{4\alpha^2-2}{\alpha^2-1} - 2\nu_m - g(\alpha)\left(1-2\nu_m+\frac{3\alpha^2}{\alpha^2-1}\right)\right]\\
S_{2222} = S_{3333} &= \frac{1}{4(1-\nu_m)}\left[\frac{3\alpha^2}{2(\alpha^2-1)} + g(\alpha)\left(1-2\nu_m-\frac{9}{4(\alpha^2-1)}\right)\right]\\
S_{1122} = S_{1133} &= \frac{1}{2(1-\nu_m)}\left[-\frac{\alpha^2}{\alpha^2-1} + 2\nu_m + g(\alpha)\left(1-2\nu_m+\frac{3}{2(\alpha^2-1)}\right)\right]\\
S_{2211} = S_{3311} &= \frac{1}{2(1-\nu_m)}\left[-\frac{\alpha^2}{\alpha^2-1} + \frac{g(\alpha)}{2}\left(\frac{3\alpha^2}{\alpha^2-1} - (1-2\nu_m)\right)\right]\\
S_{2233} = S_{3322} &= \frac{1}{4(1-\nu_m)}\left[\frac{\alpha^2}{2(\alpha^2-1)} - g(\alpha)\left(1-2\nu_m+\frac{3}{4(\alpha^2-1)}\right)\right]\\
S_{1212} = S_{1313} &= \frac{1}{4(1-\nu_m)}\left[-\frac{2}{\alpha^2-1} - 2\nu_m - \frac{g(\alpha)}{2}\left(1-2\nu_m-\frac{3(\alpha^2+1)}{\alpha^2-1}\right)\right]\\
S_{2323} &= \frac{S_{2222}-S_{2233}}{2}
\end{aligned}
\tag{A.1}
$$

where $g(\alpha)$ is a function given by

$$
g(\alpha) = \frac{\alpha}{(\alpha^2-1)^{3/2}}\left[\alpha(\alpha^2-1)^{1/2} - \cosh^{-1}\alpha\right] \tag{A.2}
$$

for prolate ellipsoidal inclusions ($\alpha > 1$) and by

$$
g(\alpha) = \frac{\alpha}{(1-\alpha^2)^{3/2}}\left[\cos^{-1}\alpha - \alpha(1-\alpha^2)^{1/2}\right] \tag{A.3}
$$

for oblate ones ($\alpha < 1$). The Eshelby's tensor has the minor symmetries; all other components are nil. ν_m stands for the Poisson's ratio of the elastic and isotropic matrix, which is replaced by the secant Poisson's ratio, ν_m^s, in the secant approach to compute the nonlinear deformation of the composite. ν_m^s can be computed from the matrix bulk modulus, k_m and the secant shear modulus, μ_m^s, as

$$v_m^s = \frac{3k_m - 2\mu_m^s}{6k_m + 2\mu_m^s} \tag{A.4}$$

The partial derivatives of the components of Eshelby's tensor with respect to v_m are given by

$$\begin{aligned}
\frac{\partial S_{1111}}{\partial v_m} &= \frac{2\alpha^2 - g(\alpha)(1+2\alpha^2)}{2(-1+v_m)^2(-1+\alpha^2)} \\
\frac{\partial S_{2222}}{\partial v_m} &= \frac{\partial S_{3333}}{\partial v_m} = \frac{6\alpha^2 - g(\alpha)(5+4\alpha^2)}{16(-1+v_m)^2(-1+\alpha^2)} \\
\frac{\partial S_{1122}}{\partial v_m} &= \frac{\partial S_{1133}}{\partial v_m} = \frac{-4+5g(\alpha)+2\alpha^2-2g(\alpha)\alpha^2}{4(-1+v_m)^2(-1+\alpha^2)} \\
\frac{\partial S_{2211}}{\partial v_m} &= \frac{\partial S_{3311}}{\partial v_m} = \frac{-2\alpha^2+g(\alpha)(-1+4\alpha^2)}{4(-1+v_m)^2(-1+\alpha^2)} \\
\frac{\partial S_{2233}}{\partial v_m} &= \frac{\partial S_{3322}}{\partial v_m} = \frac{2\alpha^2+g(\alpha)(-7+4\alpha^2)}{16(-1+v_m)^2(-1+\alpha^2)} \\
\frac{\partial S_{1212}}{\partial v_m} &= \frac{\partial S_{1313}}{\partial v_m} = \frac{g(\alpha)-2\alpha^2+2g(\alpha)\alpha^2}{4(-1+v_m)^2(-1+\alpha^2)}
\end{aligned} \tag{A.5}$$

Appendix B. Determination of the von Mises equivalent stress in the second order method

Kreher (1990) and Buryachenko (1996) demonstrated that $\hat{\bar{\sigma}}_m^{eq}$ can be computed directly from the secant compliance tensor of the composite according to

$$\hat{\bar{\sigma}}_m^{eq} = \left[\frac{3}{1-\xi}\bar{\boldsymbol{\sigma}}\frac{\partial \boldsymbol{M}^s}{\partial(1/\mu_m^s)}\bar{\boldsymbol{\sigma}}\right]^{1/2} \tag{B.1}$$

The secant compliance tensor of a two phase composite is given by

$$\boldsymbol{M}^s = \boldsymbol{M}_m^s + \xi(\boldsymbol{M}_i - \boldsymbol{M}_m^s)\boldsymbol{B}_i^s \tag{B.2}$$

and its derivative in relation to the secant shear compliance of the matrix can be expressed as

$$\frac{\partial \boldsymbol{M}^s}{\partial(1/\mu_m^s)} = -(\mu_m^s)^2\left[\frac{\partial \boldsymbol{M}_m^s}{\partial \mu_m^s}(\boldsymbol{I} - \xi\boldsymbol{B}_i^s) + \xi(\boldsymbol{M}_i - \boldsymbol{M}_m^s)\frac{\partial \boldsymbol{B}_i^s}{\partial \mu_m^s}\right] \tag{B.3}$$

in terms of the derivatives of the secant compliance tensor of the matrix and of the secant stress concentration tensor of the inclusion. Assuming that $\boldsymbol{B}_i^s$ is given by the Mori-Tanaka method (Eq. (11)), the derivative in relation to the secant shear modulus of the matrix is

$$\frac{\partial \boldsymbol{B}_i^s}{\partial \mu_m^s} = -(1-\xi)\boldsymbol{B}_i^s\left\{\left[2\boldsymbol{K}(\boldsymbol{I} - \boldsymbol{S}_m^s) - \boldsymbol{L}_m^s\frac{\partial \boldsymbol{S}_m^s}{\partial \mu_m^s}\right](\boldsymbol{M}_i - \boldsymbol{M}_m^s) + \boldsymbol{L}_m^s(\boldsymbol{I} - \boldsymbol{S}_m^s)\left(\frac{1}{2\mu_m^s}\right)^2\boldsymbol{K}\right\}\boldsymbol{B}_i^s \tag{B.4}$$

where $\boldsymbol{L}_m^s = (\boldsymbol{M}_m^s)^{-1}$ and the derivative of Eshelby's tensor in relation to μ_m^s is given by

$$\frac{\partial \boldsymbol{S}_m^s}{\partial \mu_m^s} = \frac{\partial v_m^s}{\partial \mu_m^s}\frac{\partial \boldsymbol{S}_m^s}{\partial v_m^s} = -\frac{9k_m}{2(3k_m + \mu_m^s)}\frac{\partial \boldsymbol{S}_m^s}{\partial v_m^s} \tag{B.5}$$

where the partial derivatives of Eshelby's tensor in relation to v_m^s can be found in Appendix A. Eqs. (B.4) and (B.5) are introduced in Eq. (B.1) to obtain the von Mises equivalent stress in the matrix.

References

Abaqus, 2005. Users' Manual. Hibbitt, Karlsson, and Sorensen, Inc.

Benveniste, Y., 1987. A new approach to the application of Mori-Tanaka's theory in composite materials. Mechanics of Materials 6, 147–157.

Berveiller, M., Zaoui, A., 1979. An extension of the self-consistent scheme to plastically-flowing polycrystals. Journal of the Mechanics and Physics of Solids 26, 325–344.

Buryachenko, V.A., 1996. The overall elastoplastic behavior of multiphase materials with isotropic components. Acta Mechanica 119, 93–117.

Chaboche, J.L., Kanouté, P., Roos, A., 2005. On the capabilities of mean-field approaches for the description of plasticity in metal-matrix composites. International Journal of Plasticity 21, 1409–1434.

DIGIMAT, 2005. A software for the linear and nonlinear multi-scale modeling of heterogeneous materials. e-Xstream engineering, Louvain-la-Neuve, Belgium.

Doghri, I., Ouaar, A., 2003. Homogenization of two-phase elasto-plastic composite materials and structures: study of tangent operators, cyclic plasticity and numerical algorithms. International Journal of Solids and Structures 40, 1681–1712.

Eshelby, J.D., 1957. The determination of the elastic field of an ellipsoidal inclusion and related problems. Proceedings of the Royal Society of London A252, 376–396.

Gilormini, P., 1995. Insuffisance de l'extension classique du modèle auto-cohérent au comportement non linéaire. Comptes rendus de l Academie des Sciences, Paris. Serie IIb 320, 115–122.

González, C., LLorca, J., 2000. A self-consistent approach to the elasto-plastic behavior of two-phase materials including damage. Journal of the Mechanics and Physics of Solids 48, 675–692.

González, C., Segurado, J., LLorca, J., 2004. Numerical simulation of elasto-plastic deformation of composites: evolution of stress microfields and implications for homogenization models. Journal of the Mechanics and Physics of Solids 52, 1573–1593.

Gusev, A.A., Hine, P.J., Ward, I.M., 2000. Fiber packing and elastic properties of a transversely random unidirectional glass/epoxy composite. Composites Science and Technology 60, 533–541.

Hazanov, S., Huet, C., 1994. Order relationships for boundary condition effects in heterogeneous bodies smaller than the representative volume. Journal of the Mechanics and Physics of Solids 42, 1995–2011.

Hill, R., 1965. A self-consistent mechanics of composite materials. Journal of the Mechanics and Physics of Solids 13, 213–222.

Hine, P.J., Lusti, H.R., Gusev, A.A., 2002. Numerical simulation of the effects of volume fraction, aspect ratio and fibre length distribution on the elastic and thermoelastic properties of short fibre composites. Composites Science and Technology 62, 1445–1453.

Hutchinson, J.W., 1970. Elastic–plastic behavior of polycrystalline metals and composites. Proceedings of the Royal Society of London A319, 247–272.

Kreher, W., 1990. Residual stresses and stored elastic energy of composites and polycrystals. Journal of the Mechanics and Physics of Solids 38, 115–128.

Lin, A., Han, S.-P., 2002. On the distance between two ellipsoids. SIAM Journal on Optimization, 298–308.

LLorca, J., Segurado, J., 2004. Three-dimensional multiparticle cell simulations of deformation and damage in sphere-reinforced composites. Materials Science and Engineering A365, 267–274.

Masson, R., Bornert, M., Suquet, P., Zaoui, A., 2000. An affine formulation for the prediction of the effective properties of non linear composites and polycrystals. Journal of the Mechanics and Physics of Solids 48, 1203–1227.

Masson, R., Zaoui, A., 1999. Self-consistent estimates for the rate dependent elastoplastic behavior of polycrystalline materials. Journal of the Mechanics and Physics of Solids 47, 1543–1568.

Monetto, I., Drugan, W.J., 2004. A micromechanics-based nonlocal constitutive equation for elastic composites containing randomly oriented spheroidal heterogeneities. Journal of the Mechanics and Physics of Solids 52, 359–393.

Nemat-Nasser, S., Hori, M., 1999. Micromechanics: Overall Properties of Heterogeneous Materials. North-Holland.

NETGEN, 2004. A 3D Tetrahedral mesh generator—Version 4.4. NETGEN.

Petterman, H.E., Planskensteiner, A.F., Böhm, H.J., Rammerstorfer, F.G., 2002. A termo-elasto-plastic constitutive law for inhomogeneous materials based on an incremental Mori-Tanaka approach. Computers and Structures 71, 197–214.

Pierard, O., LLorca, J., Segurado, J., Doghri, I., 2007. Micromechanics of particle-reinforced elasto-viscoplastic composites: numerical simulations versus affine homogenization. International Journal of Plasticity 23, 1041–1060.

Ponte-Castañeda, P., 1991. The effective mechanical properties of nonlinear isotropic composites. Journal of the Mechanics and Physics of Solids 39, 45–71.

Ponte-Castañeda, P., Suquet, P., 1998. Nonlinear composites. Advances in Applied Mechanics 34, 171–301.

Qiu, Y., Weng, G., 1992. A theory of plasticity for porous and particle-reinforced composites. Journal of Applied Mechanics 59, 261–268.

Rintoul, M.D., Torquato, S., 1997. Reconstruction of the structure of dispersions. Journal of Colloid and Interface Science 186, 467–476.

Segurado, J., González, C., LLorca, J., 2003. A numerical investigation of the effect of particle clustering on the mechanical properties of composites. Acta Materialia 51, 2355–2369.

Segurado, J., LLorca, J., 2002. A numerical approximation to the elastic properties of sphere-reinforced composites. Journal of the Mechanics and Physics of Solids 50, 2107–2121.

Segurado, J., LLorca, J., 2005. A computational micromechanics study of the effect of interface decohesion on the mechanical behavior of composites. Acta materialia 53, 4931–4942.

Segurado, J., LLorca, J., 2006. Computational micromechanics of composites: the effect of particle spatial distribution. Mechanics of Materials 38, 873–883.

Segurado, J., LLorca, J., González, C., 2002. On the accuracy of mean-field approaches to simulate the plastic deformation of composites. Scripta Materialia 46, 525–529.

Suquet, P., 1995. Overall properties of non-linear composites: a modified secant moduli theory and its link with ponte castañeda's nonlinear variational procedure. Comptes rendus de l Academie des Sciences, Paris. Serie IIb 320, 563–571.

Suquet, P., 1997. Effective properties of nonlinear composites. In: Continuum Micromechanics. CISM Course and Lecture Notes. pp. 197–264.

Tandon, G.P., Weng, G.J., 1988. A theory of particle-reinforced plasticity. Journal of Applied Mechanics 55, 126–135.

Torquato, S., 2001. Random heterogeneous materials. Springer.